Ab initio and machine-learning study of surface energetics in $Be_{12}Ti$

D.V. Bachurin, C. Stihl, P.V. Vladimirov

Institute for Applied Materials – Applied Materials Physics, Karlsruhe Institute of Technology,
Hermann-von-Helmholtz-Platz 1, 76344, Eggenstein-Leopoldshafen, Germany

Abstract

A comprehensive *ab initio* study of the surface energetics of the intermetallic compound $Be_{12}Ti$ was performed, focusing on 24 low-index crystallographic planes (*hkl* with maximal Miller index ≤ 3) and their non-equivalent surface terminations. To enable accurate calculation of surface energies for non-stoichiometric slabs, a machine-learning interatomic potential was developed and trained on energies and atomic forces obtained by *ab initio*. Surface-layer relaxations are found to be strongly termination dependent, exhibiting complex inward and outward atomic displacements. Surface energies are influenced more significantly by surface termination than by crystallographic orientation, particularly for low-index planes. Surfaces with maximum Miller index one display pronounced termination dependence, while higher-index surfaces exhibit smaller variations. For a fixed crystallographic orientation, the dependence of surface energy on surface termination follows an invariant trend: the minimum surface energy corresponds to titanium-terminated surfaces, whereas the surface energy increases as titanium atoms are located at greater distances from the surface plane. Wulff constructions demonstrate that equilibrium crystal and void shapes are highly sensitive to termination-dependent surface energies. This work presents a high-throughput framework for surface modeling in multicomponent compounds based on machine-learning interatomic potentials. The approach establishes the groundwork for subsequent assessment of tritium retention at $Be_{12}Ti$ surfaces, which is an essential step toward quantifying tritium inventories in neutron multiplier components of fusion reactors.

Keywords: ab initio calculations; titanium beryllide; surface energy; machine-learned potential

Corresponding author: D.V. Bachurin
Email address: dmitry.bachurin@kit.edu

ORCID Ids: D.V. Bachurin: 0000-0001-8995-211X
P.V. Vladimirov: 0000-0003-2358-6043

1. Introduction

Understanding the structure and energetics of free surfaces in intermetallic compounds is of both fundamental and practical importance, as surface properties critically determine the behavior of materials under extreme conditions (e.g., irradiation, corrosion, and high-temperature environments), influencing a wide range of material characteristics like surface diffusion [1, 2], adsorption [3-5], segregation [6], corrosion resistance [7-9] and radiation-induced damage evolution [10-12]. In intermetallic compounds relevant to nuclear technology, the behavior of free surfaces plays a key role in processes such as defect migration, bubble formation, and the retention or release of tritium.

The study of intermetallic surfaces presents significant challenges due to their complex atomic arrangements and the coexistence of different types of chemical bonding. Unlike pure metals, intermetallic compounds often exhibit anisotropic surface energies and multiple non-equivalent atomic terminations, even for the same crystallographic plane orientation. This structural and chemical complexity makes it difficult to predict surface stability and reconstruction phenomena based solely on empirical models. Therefore, modeling based on *ab initio* and molecular dynamics methods plays a crucial role for exploring the properties and evolution of intermetallic surfaces.

Ab initio methods, typically within the framework of density functional theory, provide accurate insights into fundamental surface characteristics, including surface energies, atomic relaxations, and electronic structure. These first-principles approaches allow a quantitative description of surface stability and reconstruction, as well as the identification of energetically favorable terminations and adsorption sites. Molecular dynamics approach, on the other hand, enables the investigation of dynamic processes occurring at finite temperatures, such as surface diffusion, defect nucleation, and the interaction of surfaces with impurities or irradiation-induced defects over extended time and length scales. When combined, these two methods form a comprehensive multiscale framework that bridges the gap between electronic-level interactions and macroscopic material behavior, thereby providing a deeper understanding of the thermodynamic stability and kinetic evolution of complex intermetallic surfaces.

Beryllides, particularly the intermetallic compound $Be_{12}Ti$, have attracted growing attention in recent years as advanced neutron multiplier materials for nuclear fusion applications, offering a promising alternative to pure beryllium [13-17]. $Be_{12}Ti$ exhibits several advantages, including a higher melting point (~1866 K vs. 1560 K for pure beryllium), enhanced oxidation resistance, lower swelling under neutron irradiation, reduced tritium retention, and good compatibility with structural materials. These properties make it a safer and more cost-effective candidate for replacing pure beryllium in helium-cooled pebble bed (HCPB) blanket designs [14].

Under neutron irradiation, beryllium nuclei in beryllides undergo transmutation into tritium and helium, accompanied by the formation of point defects and their clusters. At elevated temperatures, tritium diffuses and can be trapped at these defects, leading to the nucleation and growth of gas bubbles. Although tritium concentration is significantly lower than that of helium and thus does not notably alter the microstructure, its radioactivity represents a major safety concern. Consequently, assessing tritium retention in beryllides is essential for the safe operation and decommissioning of breeding blanket materials.

A quantitative understanding of how much tritium can be accumulated at the free surfaces of irradiation-induced bubbles requires a detailed characterization of the surface energetics of $Be_{12}Ti$. Identifying the most energetically favorable surface orientations and terminations is crucial, as these determine the morphology and trapping capacity of the bubbles. The present work addresses this problem by performing *ab initio* calculations of the surface energies of $Be_{12}Ti$ for a set of low-index crystallographic planes, characterized by the Miller

indices (hkl) with $\max(h,k,l) \leq 3$, considering all their non-equivalent terminations. Thus, obtained data serve as a training set for the development of a machine-learning interatomic potential for Be-Ti system, which is essential for accurately modeling large-scale structures beyond the reach of direct *ab initio* calculations. The results provide fundamental insight into the energetical hierarchy of these surfaces and form a basis for future studies of tritium interaction, retention, and release.

2. Methodology

2.1. Crystal structure of $Be_{12}Ti$

The crystal structure of titanium beryllide $Be_{12}Ti$ is significantly more complex than the hexagonal close-packed lattices of its constituent elements, beryllium and titanium. $Be_{12}Ti$ adopts a tetragonal lattice within the *I*4/*mmm* space group, featuring four crystallographically non-equivalent atomic sites: three occupied by beryllium atoms – Be1 at the [8f] Wyckoff position (0, 0.218, 0.5), Be2 at the [8i] (0, 0.351, 0), and Be3 at the [8j] (0.25, 0.25, 0.25) positions, and one occupied by titanium, Ti1, at the [2a] position (0, 0, 0). These positions are defined by their Wyckoff symbols and fractional coordinates. The optimized lattice parameters are $a = b = 7.324$ Å, $c = 4.151$ Å, with angles $\alpha = \beta = \gamma = 90°$. These values slightly differ from those reported in the previous works [18, 19], primarily due to the use of an enhanced computational framework, incorporating a higher plane-wave cut-off energy and a denser *k*-point grid.

2.2. Surfaces in $Be_{12}Ti$

All crystallographically distinct surfaces consistent with the crystal symmetry of $Be_{12}Ti$ were considered. Specifically, five surfaces with a maximum Miller index of 1, seven with a maximum index of 2, and seventeen with a maximum index of 3 were analyzed (see Table 1). In addition to the crystallographic orientation, $Be_{12}Ti$ surfaces exhibit multiple non-equivalent atomic terminations for the same crystallographic plane, each characterized by a unique atomic arrangement and surface composition. This behavior arises from the complex non-Bravais crystal structure of the compound and the presence of chemically distinct atomic layers composed of beryllium and titanium atoms within the unit cell. Previous studies on various intermetallic compounds have demonstrated that such terminations can exhibit significant differences in surface energy, atomic relaxation, and electronic structure [3, 20-24]. Therefore, the effect of surface termination must be carefully considered when evaluating the overall surface stability and morphology of $Be_{12}Ti$.

Our analysis revealed that the number of possible terminations for the studied low-index surfaces ranges from two to eight. Representative examples of two different terminations for (110) and (102) surfaces are shown in Fig. 1. The (311) surface was found to possess twelve non-equivalent terminations. To ensure consistency in the classification of surface terminations, a clear criterion was adopted: two atomic planes were considered distinct if the difference in their atomic coordinates along the direction normal to the given crystallographic plane exceeded 0.01 Å; otherwise, they were treated as belonging to the same layer. This definition helps to avoid artificial duplication of terminations arising from negligible atomic separations that fall within the computational uncertainty of the method.

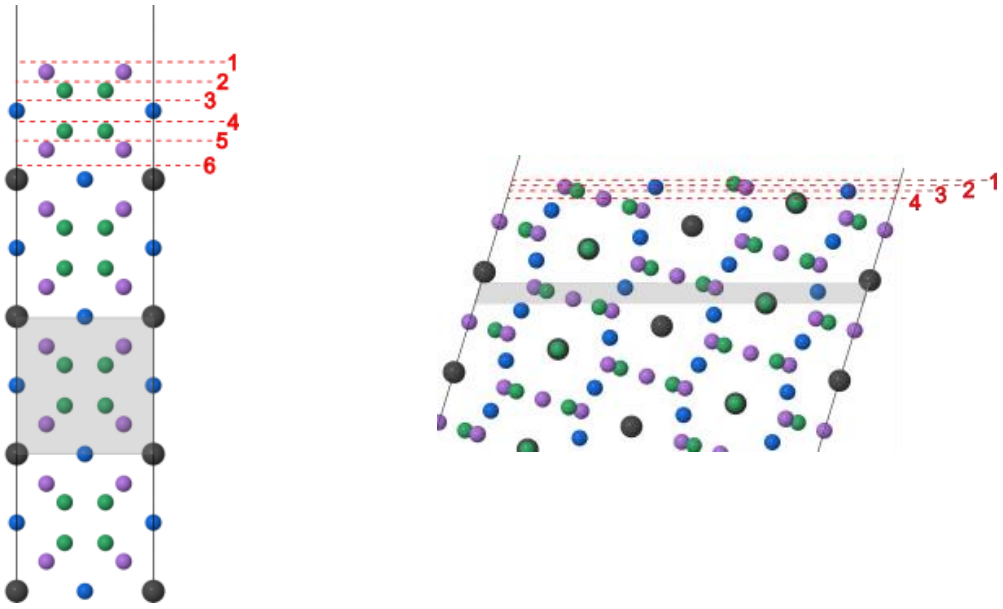

(a) (b)

Fig. 1. The side views of the (a) (110) and (b) (102) surfaces of $Be_{12}Ti$ illustrating possible non-equivalent terminations (labeled by numbers). Atoms are colored according to their chemical species and Wyckoff positions: large dark grey spheres represent titanium atoms, while blue, green and violet spheres denote three symmetrically non-equivalent beryllium atoms. The gray lines indicate the periodic repeat unit specific to each surface orientation. Only a part of the computational cell is presented for clarity.

2.3. Construction of slabs

Atomic slab configurations were generated using the SlabGenerator class from the pymatgen.core.surface module [25, 26]. This tool constructs an oriented unit cell in which the lattice vectors **a** and **b** lie in the (*hkl*) plane, while **c** is perpendicular to the surface. The implemented algorithm aims to produce oriented unit cells with minimal surface area. However, for several high-index surfaces the algorithm failed, yielding configurations containing more than 400 atoms. Because structural relaxation of such large systems for all possible terminations would require prohibitively large computational time, these slabs were initially excluded from the training set. After correcting this issue, the configurations were regenerated with reduced surface areas and subsequently included in the validation set.

To identify and label stacking sequences of atomic layers for each surface orientation, the standard module was extended with custom routines developed in this work. Each atomic layer is uniquely characterized not only by its chemical composition but also by the Wyckoff labels of the atoms. This approach makes it possible to distinguish between beryllium atoms in different local environments, which is essential for calculations using machine-learned potentials. It should be noted that the adopted labeling scheme differentiates atomic layers only within a given surface orientation. Labels assigned to different orientations (A, B, C, …) are defined independently and therefore cannot be directly compared across orientations.

Two approaches can be used to construct slabs with multiple terminations: (i) symmetric slabs with identical terminations on both surfaces, which may deviate from the bulk stoichiometry, and (ii) asymmetric slabs that preserve the stoichiometric composition. In this work, the first approach was adopted because it enables direct calculation of the surface energy for each termination, which is the primary objective. The second approach is more suitable for evaluating the cleavage energy along a given termination.

A drawback of symmetric slabs is the deviation from bulk stoichiometry. As discussed in the next section, the surface energy of a symmetric but non-stoichiometric slab depends on the chemical potential of the constituent species. Strictly speaking, atoms of the same chemical element occupying different Wyckoff positions should be treated as distinct species. However, *ab initio* calculations provide only the total energy per compositional unit, making it impossible to extract individual chemical potentials for each species from the stoichiometric bulk crystal. To address this limitation, a machine-learning interatomic potential was developed for classical molecular dynamics simulations, trained on *ab initio* data obtained for a wide range of free surfaces. The resulting potential enables decomposition of the total lattice energy into element-specific contributions from beryllium and titanium, thus allowing the determination of the chemical potentials necessary for calculating the surface energy. The framework for machine-learned potential development is described in Section 2.6.

2.4. Calculation of surface energy

The surface energy, γ, represents the excess energy per unit area required to create a surface from the bulk crystal. Within the slab model approach, γ is determined from the total energy difference between a slab containing two free identical surfaces (symmetric slab) and an equivalent number of atoms in the bulk:

$$\gamma = \frac{1}{2A}(E_{slab} - N \cdot E_{bulk}), \tag{1}$$

where E_{slab} is the total energy of the slab, E_{bulk} is the energy per atom in the bulk crystal, N is the number of atoms in the slab, and A is the surface area of one surface of the slab. The factor of 2 accounts for two equivalent surfaces in a symmetric slab model. For a single-element material Eq. (1) is sufficient when both slab surfaces are identical. If the slab surfaces are different (asymmetric slab), the surface energies of the top and bottom faces, γ_{top} and γ_{bottom} can be obtained by constructing at least two slab configurations with different terminations and solving a set of linear equations:

$$E_{slab}^{(i)} = N^{(i)} \cdot E_{bulk} + A\left(\gamma_{top}^{(i)} + \gamma_{bottom}^{(i)}\right), \tag{2}$$

where upper index i denotes different slab configurations.

For systems composed of two or more elements, the surface energy depends on the chemical potential of the constituent species. In this case, the surface energy is computed as

$$\gamma(\mu_i) = \frac{1}{2A}(E_{slab} - \textstyle\sum_i N_i\mu_i), \tag{3}$$

where N_i is the number of atoms of species i in the slab, and μ_i is the chemical potential of species i in stoichiometric crystal. For a binary system $Be_{12}Ti$, Eq. (3) become:

$$\gamma(\mu_{Be}, \mu_{Ti}) = \frac{1}{2A}(E_{slab} - N_{Be}\mu_{Be} - N_{Ti}\mu_{Ti}), \tag{4}$$

where μ_{Be} and μ_{Ti} are the chemical potentials of one Be and Ti atom in $Be_{12}Ti$ lattice, respectively; N_{Be} and N_{Ti} are the number of Be and Ti atoms in the slab, respectively.

In the case of an asymmetric slab, i.e., when stoichiometry is preserved but the two surfaces are non-equivalent, Eq. (2) can be applied to calculate the surface energy. In this formulation, the number of atomic layers per lattice period, N, must be equal to the number of non-equivalent atomic layers, M, that is, $N = M$. This condition is satisfied, for example, in the case of alternating layers of the type of ABC…ABC, where $N = 3$ and $M = 3$. However, it does not hold for more complex surfaces, such as the (110) surface in $Be_{12}Ti$, which exhibits the stacking sequence ABCDCB…ABCDCB, where $N = 6$ and $M = 4$.

If stoichiometry is violated, that is, when the slab has identical terminations on both free surfaces, Eq. (4) should be used instead. However, this approach introduces an additional challenge: the chemical potentials μ_{Be} and μ_{Ti} of the constituent elements in $Be_{12}Ti$ are not directly known. This is because VASP provides only the total energy of the entire computational cell, without distinguishing the respective contributions of beryllium and titanium atoms in the tetragonal lattice of $Be_{12}Ti$.

2.5. Ab initio modeling

All density functional theory calculations were performed using the Vienna Ab initio Simulation Package (VASP). Projector-augmented wave (PAW) pseudopotentials [27] were employed in combination with the R2SCAN meta-generalized gradient approximation (GGA) for the exchange-correlation functional [28, 29]. Pseudopotentials for beryllium (two valence electrons) and titanium (four valence electrons) were obtained from the VASP library. The structural model of the titanium beryllide $Be_{12}Ti$ was adopted from the Materials Project database (entry mp-2024836) [30], a collaborative online repository providing extensive *ab initio* data for crystalline materials. This structure was subsequently fully relaxed using the above-described pseudopotentials.

Brillouin zone sampling was conducted using an automatically generated *k*-point grid with a minimum spacing of 0.22 $Å^{-1}$ (KSPACING tag). A plane-wave basis set cut-off energy of 680 eV was applied (ENCUT tag). Convergence criteria for electronic and ionic relaxations were set to a total energy difference of less than 1.0×10^{-5} eV between consecutive electronic iterations (EDIFF tag) and residual atomic forces below 2.0×10^{-2} eV/Å (EDIFFG tag), respectively. A second-order Methfessel-Paxton smearing scheme with a width of 0.2 eV (ISMEAR and SIGMA tags) was employed to smooth the Fermi level step, resulting in negligible entropy contributions of approximately 1.0 meV per atom. The simulation cell volume and shape were fixed in all calculations following the initial structural refinement of the $Be_{12}Ti$ structure. The free surfaces are separated by a sufficiently thick vacuum layer, which effectively prevents any interaction between the two opposite surfaces caused by periodic boundary conditions. Atomic structures were visualized using the open-source molecular visualization software Jmol [31].

Surface relaxations were carried out using a two-step procedure to ensure physically meaningful atomic configurations. In the first step, one or more periodically repeated sequences of innermost atomic layers near the center of the slab were held fixed to suppress unphysically deep relaxation patterns observed in preliminary unconstrained calculations. After convergence of this constrained relaxation, all atomic positions were released in a second step, allowing unrestricted structural relaxation. The resulting configurations represent fully relaxed surface structures and were used for the subsequent evaluation of surface energetics.

2.6. Machine-learning interatomic potential for Be-Ti system

The extensive *ab initio* dataset, which includes symmetric slabs of all low-index surfaces (up to Miller index 3) and their non-equivalent terminations, served as the foundation for training a fully local E(3)-equivariant Allegro Machine-Learning Interatomic Potential (MLIAP) [32], as implemented within the NequIP framework [33, 34]. In addition to fully relaxed surface slab structures, *ab initio* molecular dynamics simulations of the perfect crystals of Be, Ti and $Be_{12}Ti$ at a temperature of 1200 K under fixed cell shape and volume, and the resulting configurations were included in the training dataset. In total, the dataset contains 3603 structures with corresponding total energies and 973394 atomic force components. The data were randomly divided into a training set consisting of 3245 structures with 875375 force components and a validation set comprising 358 structures with 98019 force components. The

slab structures corresponding to the five surface orientations (311), (213), (312), (321), and (322) were excluded from the training because their surface areas, and consequently the number of atoms in the slabs, were prohibitively large for *ab initio* calculations. After resolving the issue in their construction, their surface energies were computed using the machine-learning interatomic potential and subsequently compared with the *ab initio* results.

The Allegro architecture was retained in its high-precision default configuration, with the exception of the cut-off radius, which was set to 6.0 Å to match the default value used in earlier Allegro versions. The Allegro MLIAP employed in this work was trained for 4532 epochs using the Adam optimizer with a loss function composed of equally weighted mean squared errors of atomic forces and total energies. The final model was selected based on the lowest mean absolute error on the validation set. The resulting Allegro MLIAP demonstrates excellent predictive performance, as illustrated in Fig. 2. The strong correlation between the mean energy per atom predicted by the model and the corresponding *ab initio* values for both the training and validation datasets indicates typical absolute errors on the order of only a few meV per atom.

Training with the newly suggested default cut-off radius of 5.0 Å was found to consistently produce potentials that, despite yielding excellent total energy predictions, imply unphysical chemical potentials – strongly positive for Ti and strongly negative for Be in $Be_{12}Ti$. This behavior is attributed to the limited spatial range of a 5.0 Å cut-off, which captures primarily intra-column positional correlations of Ti atoms in the $Be_{12}Ti$ structure. In contrast, increasing the cut-off radius to 6.0 Å is sufficient to incorporate inter-column positional relationships between Ti atoms in neighboring columns, thereby providing a more complete description of the local atomic environment. As a result, the best-performing Allegro MLIAP yields physically reasonable chemical potentials of $\mu_{Be} = -5.06$ eV and $\mu_{Ti} = -6.12$ eV for Be and Ti in $Be_{12}Ti$, respectively. Note that the chemical potential of beryllium was obtained as an average over three distinct Wyckoff positions.

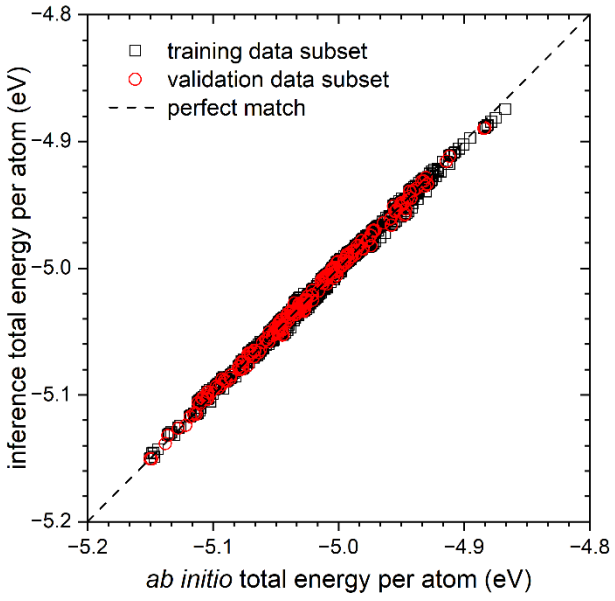

Fig. 2. Scatter plot of the full dataset, partitioned into training and validation subsets, showing predictions from the best Allegro MLIAP compared with the corresponding *ab initio* results.

3. Results and discussion

3.1. Interplanar and atomic relaxations

Relaxation of interplanar distances at free surfaces is a key factor in determining their structural and energetic stability. The creation of a free surface breaks the translational symmetry of the crystal and reduces atomic coordination, leading to a redistribution of interatomic forces. As a consequence, the interplanar spacings in the near-surface region deviate from their bulk values. These deviations typically extend over only a few atomic layers, beyond which bulk-like behavior is gradually recovered in the interior of the slab.

The magnitude and even the sign of the interlayer relaxation depend strongly on the crystallographic orientation. For pure beryllium, the close-packed surfaces $(1\bar{1}00)$, $(2\bar{1}\bar{1}0)$, $(1\bar{1}01)$, and $(2\bar{1}\bar{1}2)$ exhibit inward relaxation, characterized by a contraction of the outermost interlayer spacing [35-40]. In contrast, the (0001) surface of beryllium shows a pronounced outward relaxation relative to the bulk value [35, 36, 41, 42]. It is worth noting that this behavior differs from that of titanium, where the (0001) surface undergoes inward relaxation [43-45]. The magnitude of relaxation has been shown to correlate with surface roughness, i.e., with the degree of structural openness of a given surface orientation [46, 47].

An analysis of interplanar relaxation was carried out for the (110) and (100) surfaces, taking into account all possible terminations. For the surfaces with maximum Miller indices of 2 and 3, the distance between certain atomic planes becomes relatively small, complicating the definition of distinct atomic layers. In some cases, an atomic row within the computational cell may be represented by only a single atom per surface unit cell. When the initial interplanar spacing is small, surface relaxation can cause atoms from adjacent planes to move toward one another and nearly coincide, effectively forming a single atomic plane. This makes it difficult to distinguish between neighboring layers and can lead to ambiguities or artificially large values in the calculated interplanar spacing d_{ij}.

To quantify interplanar relaxation, the relative change in the distance between adjacent layers *i* and *j* was calculated as

$$\Delta d_{ij} = \frac{d_{ij} - d_{ij}^{bulk}}{d_{ij}^{bulk}}, \quad (5)$$

where d_{ij} is the distance between adjacent layers i and j in the slab, and d_{ij}^{bulk} is the corresponding interplanar distance in the bulk structure. Negative values of Δd_{ij} indicate inward relaxation (contraction), whereas positive values correspond to outward relaxation (expansion).

The calculated interlayer relaxations for the six outermost layers of the (110) and (100) surfaces of $Be_{12}Ti$ are summarized in Table 1. For both surfaces, termination 1 corresponds to the configuration in which titanium atoms are positioned farthest from the surface, whereas termination 6 represents the opposite extreme, with titanium atoms occupying the outermost surface layer. During relaxation of layers containing both beryllium and titanium atoms, a characteristic behavior was observed. When beryllium and titanium atoms were initially located within the same atomic plane, structural relaxation caused them to displace in opposite directions relative to that plane. In such cases, the final position of the atomic layer was defined as the average of the relaxed coordinates of all atoms originally belonging to the same plane.

The relaxation patterns for both surfaces are found to be complex and exhibit a non-systematic alternation of inward (negative) and outward (positive) relaxations. For the (110) surface, the outermost layers for all six surface terminations predominantly undergo inward relaxation. In contrast, terminations 2 and 3 of the (100) surface show outward relaxation in

the upper layers. In general, the magnitude of Δd_{ij} decreases with increasing depth from the surface and gradually approaches zero, indicating convergence toward the bulk interplanar spacing. However, some deviations from this trend are observed. For example, for termination 4 of the (100) surface, the value of Δd_{67} significantly exceeds Δd_{56}. This behavior is associated with the relatively small initial spacing between adjacent planes: structural relaxation can cause these layers to shift toward each other, and even small absolute displacements produce comparatively large relative changes in interplanar distance. A similar mechanism explains the relatively high values of Δd_{23} and Δd_{34} for termination 2 of the (100) surface. Different terminations of the same crystallographic surface exhibit distinct relaxation patterns, confirming that interplanar spacings are highly sensitive to surface termination, particularly to the identity of the outermost atomic layer and its stacking sequence. This sensitivity reflects the local redistribution of charge and interatomic forces at the surface. It is also noteworthy that some d_{ij} values are close to zero, for example, Δd_{45} for termination 6 of the (110) surface, indicating nearly bulk-like interlayer spacing at that depth.

At present, a direct comparison with experimental measurements or previously reported *ab initio* calculations of interplanar relaxation in $Be_{12}Ti$ is not possible due to the lack of available data. Nevertheless, interplanar relaxation has been extensively investigated in a number of other intermetallic compounds using first-principles methods [22, 23, 48]. These studies report similarly complex relaxation behavior, characterized by non-systematic alternation between inward and outward relaxation and by relatively large variations in interplanar spacings. Such observations suggest that pronounced, non-monotonic interlayer relaxations are a general characteristic of intermetallic surfaces, rather than an exceptional feature specific to $Be_{12}Ti$. Although no direct comparison is available, the present study allowed us to identify anomalies for certain surface orientations and terminations. These anomalies are likely associated with insufficient slab thickness. To eliminate such unphysical effects, a two-stage relaxation procedure was introduced.

Table 1. Interplanar relaxation of the six outermost layers for the two most energetically favorable (110) and (100) surfaces of $Be_{12}Ti$. Results for all possible terminations are shown. The relative change in the distance between adjacent layers was calculated using Eq. (5) and is expressed as a percentage of the corresponding bulk interplanar spacing.

Surface	termination	Δd_{12}	Δd_{23}	Δd_{34}	Δd_{45}	Δd_{56}	Δd_{67}
(110)	1	-2.46	-14.30	14.67	-7.61	0.92	0.56
	2	-28.34	-11.14	15.86	-7.56	0.30	1.37
	3	-14.08	-3.17	3.45	-0.86	-0.26	0.34
	4	-18.71	5.83	-2.00	1.30	-0.40	1.04
	5	-3.59	1.30	0.30	-0.44	-0.44	2.32
	6	-5.82	-0.80	1.68	0.03	1.39	-1.27
(100)	1	-16.79	-20.90	-0.42	-24.51	11.28	-1.47
	2	5.63	70.92	-73.85	15.49	-4.92	8.45
	3	40.42	-55.64	9.89	-5.14	10.86	1.59
	4	-28.61	-14.29	3.67	-5.36	-4.71	29.08
	5	-17.26	7.37	-18.15	10.51	15.81	-1.36
	6	-26.78	60.20	-23.90	-27.24	25.97	-6.02

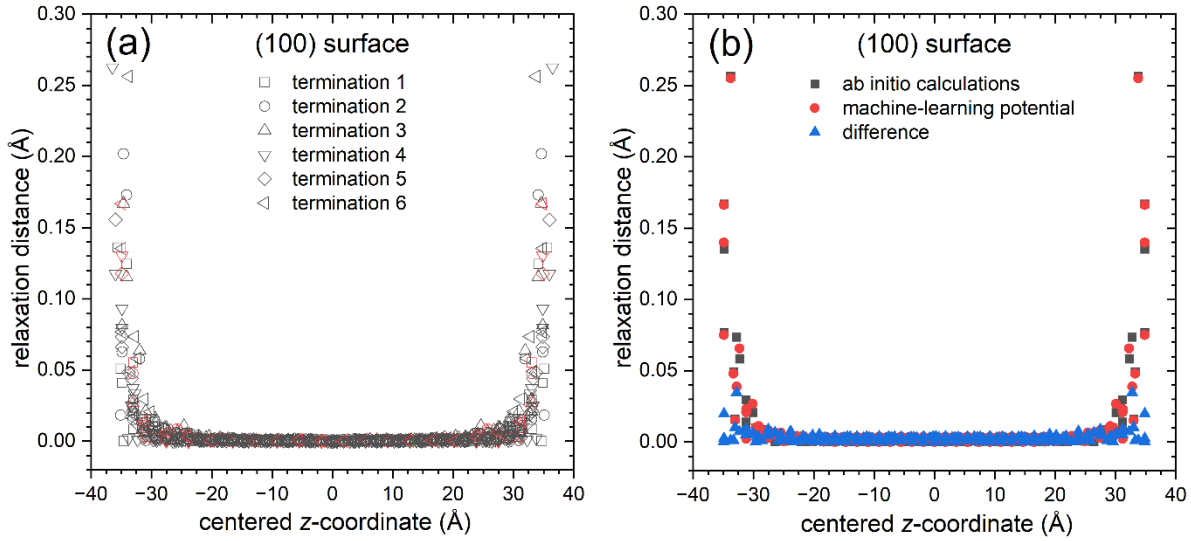

Fig. 3. (a) Atomic relaxation profiles for symmetrized slabs corresponding to the six symmetrically non-equivalent terminations of the (100) surface in $Be_{12}Ti$. Profiles are shown as the total displacement of each atom between its initial and final positions versus its initial distance from the center of the symmetric slab. Dark gray symbols denote beryllium atoms, while red symbols represent titanium atoms. (b) Comparison of relaxation profiles for termination 6 of the symmetric (100) surface obtained from *ab initio* calculations and the Allegro MLIAP potential. For clarity, the difference between the two approaches is also displayed.

Fig. 3 illustrates representative relaxation behavior using symmetrized slab models for all six symmetrically non-equivalent surface terminations for the (100) surface. The scatter plot shows the total displacement of each atom between its initial and final positions as a function of its initial distance from the center of the symmetric slab. Different terminations exhibit distinct relaxation magnitudes: beryllium atoms in terminations 4 and 6 display the largest displacements, while termination 1 shows the smallest, with terminations 2, 3, and 5 falling in between. Titanium atoms generally undergo smaller displacements than beryllium, with the maximum relaxation occurring when titanium atoms are exposed to the surface (termination 6). In all cases, atomic displacements decrease toward the slab center, where bulk-like behavior is recovered. The symmetric relaxation profiles and negligible displacements in the central region confirm that the slab thickness is sufficient to decouple the two surfaces and preserve bulk properties in the interior.

For comparison, Fig. 3b presents the relaxation profiles obtained from *ab initio* calculations and from the Allegro MLIAP for termination 6 of the (100) surface. The agreement between the two approaches is very good, with deviations not exceeding 0.5 Å. This close correspondence demonstrates that the Allegro MLIAP accurately reproduces the interlayer relaxation behavior predicted by first-principles calculations. Since the Allegro potential was trained on structural relaxations of similar character, it is expected to reliably capture surface relaxation patterns consistent with *ab initio* predictions.

3.2. Surface energy

Fig. 4 illustrates the dependence of the surface energy on the surface area, which serves as an indicator of the surface orientation, for all investigated $Be_{12}Ti$ surfaces and their crystallographically non-equivalent terminations with Miller indices up to 3. Some planes exhibit similar surface areas and therefore overlap in Fig. 4. For clarity and ease of reference,

the corresponding results are additionally summarized in Table 2, where the surfaces are listed in ascending order of surface area. Since the surface area is determined solely by the crystallographic geometry of the plane and is independent of the atomic composition, all terminations corresponding to the same surface are represented by a single abscissa value in the plot. Analysis of Fig. 4 reveals the following trends. Surfaces with a maximum Miller index of 1 exhibit a strong dependence of surface energy on surface termination, with the (110) surface showing the largest energy variation, ranging from 0.11 to 5.02 J/m^2, followed by the (100), (101), (111) and (001) surfaces. For certain surfaces with a maximum Miller index of 2, significant energy variations are also observed, such as for the (211) surface (1.51 to 3.77 J/m^2) and the (210) surface (1.68 to 3.59 J/m^2). However, the energy variations for surfaces with a maximum index of 2 are generally smaller than those for surfaces with an index of 1. For surfaces with Miller index of 3, the variation in surface energy is less pronounced, ranging from the maximal for the (310) surface (1.67 to 3.86 J/m^2) and minimal for the (113) surface (2.13 to 2.86 J/m^2). This tendency toward reduced variation is expected to persist for higher Miller indices. The lower atomic density associated with high-index surfaces decreases the contribution of titanium atoms, which provide the largest reduction in surface energy. It should be noted that the surface energy is expected to converge toward a limit value corresponding to the surface energy averaged over all possible terminations.

For additional validation, the surface energies of the (213) orientation were calculated both using *ab initio* methods and the developed Allegro MLIAP. The summary of the results is presented in Table 2 and Fig. 4, where the superscript "ML" denotes values obtained directly from the machine-learning potential. As can be seen, the surface energies for all four non-equivalent terminations of the (213) surface are reproduced with high accuracy by the MLIAP. The maximum deviation from the *ab initio* reference values does not exceed 0.004 eV per atom, indicating that the fitted potential accurately reproduces the surface energies of different terminations, even for surfaces that were not explicitly included in the training dataset. The surface energies of the (311), (312), (321), and (322) crystallographic orientations are found to be comparable in magnitude to those of other surfaces with maximum Miller index not exceeding 3. This suggests that these higher-index planes in $Be_{12}Ti$ do not introduce exceptionally high energetic penalties and may contribute to the equilibrium crystal morphology.

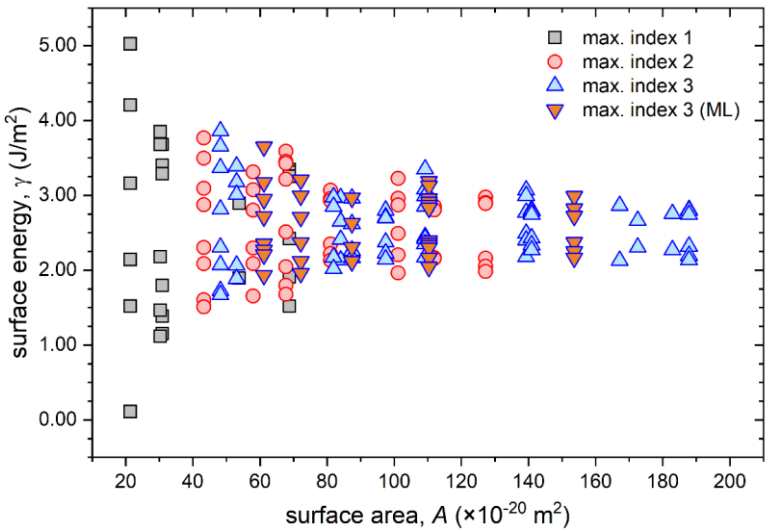

Fig. 4. Summary of the results for the low-index $Be_{12}Ti$ surfaces studied, sorted by increasing surface area. Different terminations of the same surface are plotted at the same abscissa on the graph, as they share the same surface area. The superscript "ML" denotes results obtained using a machine-learning interatomic potential.

Table 2. Summary of calculated surface energies (in J/m²) for all crystallographic planes of $Be_{12}Ti$ with Miller indices ranging from 1 to 3. For each surface orientation, N_{min} - N_{max} denotes the range between minimum and maximum number of atoms in the corresponding slab, A (in $\times 10^{-20}$ m²) represents the surface area, and $\bar{\gamma}$ is the energy averaged over all terminations of a given orientation. The planes are sorted in order of increasing surface area. A dash (–) indicates that the corresponding termination does not exist. The superscript "ML" denotes results obtained using the Allegro MLIAP. The (213) surface has twelve non-equivalent terminations, which are presented in two rows: terminations 1-8 are listed in the first row, while terminations 9-12 are given in the second row and indicated by superscript symbols in brackets.

Surface	N_{min} - N_{max}	A	Surface energy of termination								
			1	2	3	4	5	6	7	8	$\bar{\gamma}$
(110)	119-128	21.41	5.02	4.21	3.16	2.14	1.52	0.11	–	–	2.69
(100)	251-256	30.28	3.78	3.67	3.84	2.18	1.46	1.12	–	–	2.68
(101)	121-126	30.89	3.67	3.40	3.29	1.79	1.38	1.15	–	–	2.45
(001)	251-256	53.86	2.89	1.89	–	–	–	–	–	–	2.39
(111)	300-311	68.81	3.34	3.31	3.25	2.42	1.91	1.52	–	–	2.63
(211)	171-180	43.26	3.77	3.50	3.09	2.87	2.30	2.09	1.61	1.51	2.59
(112)	119-128	57.96	3.31	3.07	2.80	2.30	2.09	1.65	–	–	2.54
(210)	248-259	67.71	3.59	3.45	3.43	3.21	2.51	2.04	1.80	1.68	2.71
(201)	303-308	81.05	3.07	2.96	2.93	2.35	2.22	2.13	–	–	2.61
(221)	300-311	101.18	3.22	2.96	2.87	2.49	2.21	1.96	–	–	2.62
(102)	252-255	111.90	2.86	2.80	2.17	2.16	–	–	–	–	2.50
(212)	300-311	127.24	2.97	2.90	2.89	2.16	2.05	1.98	–	–	2.49
(310)	238-256	95.76	3.86	3.66	3.37	2.81	2.31	2.07	1.72	1.67	2.68
(301)	294-304	105.61	3.39	3.18	3.01	2.07	1.88	1.89	–	–	2.57
(320)	326-337	109.18	3.35	3.08	2.99	2.85	2.44	2.42	2.35	2.17	2.71
(331)	352-363	139.31	3.07	2.99	2.77	2.49	2.40	2.18	–	–	2.65
(302)	355-360	140.92	2.8	2.79	2.74	2.43	2.34	2.27	–	–	2.56
(103)	294-304	164.41	2.97	2.85	2.17	2.02	–	–	–	–	2.50
(113)	300-311	167.17	2.86	2.13	–	–	–	–	–	–	2.50
(332)	238-256	167.66	2.97	2.65	2.41	2.13	–	–	–	–	2.54
(203)	279-280	172.57	2.66	2.30	–	–	–	–	–	–	2.48
(223)	330-333	182.89	2.75	2.27	–	–	–	–	–	–	2.51
(313)	300-311	187.83	2.81	2.80	2.74	2.32	2.19	2.13	–	–	2.50
(323)	342-360	195.02	2.80	2.71	2.69	2.37	2.23	2.15	–	–	2.49
$(311)^{ML}$	978-1011	329.60	3.18	3.12	2.95	2.91	2.87	2.83	2.39	2.36	
$(311)^{ML}$	978-1011	329.60	$2.33^{(9)}$	$2.30^{(10)}$	$2.16^{(11)}$	$2.04^{(12)}$					2.62
(213)	528-564	350.41	2.96	2.62	2.26	2.16	–	–	–	–	2.50
$(213)^{ML}$	528-564	350.41	2.96	2.62	2.30	2.11	–	–	–	–	2.50
$(321)^{ML}$	1182-1236	365.24	3.65	3.17	2.94	2.71	2.35	2.27	2.21	1.93	2.65
$(312)^{ML}$	1026-1080	432.41	3.20	2.99	2.71	2.37	2.12	1.96	–	–	2.56
$(322)^{ML}$	1056-1089	460.15	2.99	2.82	2.72	2.37	2.25	2.16	–	–	2.55

Analysis of the atomic configurations indicates that surfaces terminated with titanium atoms exhibit minimal surface energy (termination 6 in Fig. 1). Conversely, when titanium atoms are located at the maximum distance from the free surface, which corresponds to the maximum thickness of beryllium atomic layers (termination 1 in Fig. 1), the surface energy is maximized. As beryllium atomic layers are successively removed, the surface energy gradually decreases and reaches a minimum when titanium atoms become exposed at the surface. This indicates that the presence of titanium atoms at the surface strongly influences its energetic characteristics. Consequently, this behavior explains the reduction in surface-energy variation with increasing surface area, as shown in Fig. 3. As the Miller index of a crystallographic plane increases, the surface area of the unit cell typically grows, leading to a lower surface density of titanium atoms. As a result, their contribution to the surface energy becomes less pronounced.

Furthermore, across various terminations, the maximum depth of titanium atoms beneath the surface decreases for high-index crystallographic planes. This effect also contributes to the reduced variation of surface energy with respect to the titanium depth.

Similar behavior, in which the preferential presence of one constituent element at the surface leads to a significant reduction in surface energy, has been reported for a variety of intermetallic compounds [21, 49-52]. This tendency, however, is not universal and depends on multiple factors, including the chemical nature of the constituent elements, their relative electronegativities and atomic sizes, the specific surface geometry, and the underlying crystal structure of the intermetallic phase. As a result, the energetic preference for a particular surface composition arises from a delicate balance between broken bonds, local atomic relaxations, and electronic effects, underscoring that surface stability in intermetallics is governed by a complex interplay of chemical and structural factors rather than by composition alone.

At first glance, the large variation in surface energy for a single crystallographic orientation may appear physically unjustified. However, a more detailed analysis shows that this is not the case, as discussed in the following section.

3.3. Energy of crystal cleavage

The present section considers the energy required to cleave a $Be_{12}Ti$ crystal along a given crystallographic plane. This quantity corresponds to the excess energy of asymmetric slabs. Such slabs were not investigated using *ab initio* methods in this work, since the analysis focuses on their symmetric counterparts.

Consider, for instance, the (110) surface, which exhibits the largest variation in surface energy depending on the termination, including one termination whose surface energy is close to zero. The (110) surface consists of four non-equivalent atomic layers, denoted A, B, C, and D. In a perfect bulk structure, these layers follow the stacking sequence ABCDCB:ABCDCB, where the colon indicates periodic repetition of the stacking unit. For definiteness, layer A contains titanium atoms and corresponds to the lowest surface energy, while layers B, C, and D are composed of beryllium atoms (see Fig. 1 for details). When the perfect lattice of $Be_{12}Ti$ is cleaved along the (110) plane, three distinct cutting planes are possible, resulting in six non-equivalent terminations, as illustrated schematically below.

$$\underset{6}{\overset{term}{|}} \quad \leftrightarrow \quad \underset{1}{\overset{term}{|}} \qquad \ldots : ABCDCB : A \qquad BCDCB : ABCDCB : \ldots \tag{5}$$

$$\underset{5}{\overset{term}{|}} \quad \leftrightarrow \quad \underset{2}{\overset{term}{|}} \qquad \ldots : ABCDCB : AB \qquad CDCB : ABCDCB : \ldots \tag{6}$$

$$\underset{4}{\overset{term}{|}} \quad \leftrightarrow \quad \underset{3}{\overset{term}{|}} \qquad \ldots : ABCDCB : ABC \qquad DCB : ABCDCB : \ldots \tag{7}$$

$$\underset{3}{\overset{term}{|}} \quad \leftrightarrow \quad \underset{4}{\overset{term}{|}} \qquad \ldots : ABCDCB : ABCD \qquad CB : ABCDCB : \ldots \tag{8}$$

$$\underset{2}{\overset{term}{|}} \quad \leftrightarrow \quad \underset{5}{\overset{term}{|}} \qquad \ldots : ABCDCB : ABCDC \qquad B : ABCDCB : \ldots \tag{9}$$

$$\begin{matrix} & & term & & term & \\ \ldots:ABCDCB:ABCDCB & | & \leftrightarrow & | & :ABCDCB:\ldots \\ & & 1 & & 6 & \end{matrix} \quad (10)$$

This implies that if termination 6 with the lowest surface energy of 0.11 eV forms on one side of the crystal, then the opposite side will necessarily exhibit the corresponding high-energy termination 1 with the surface energy of 5.02 eV. Analogously, terminations 5 and 2, as well as 4 and 3, are paired in a similar manner when the crystal is cleaved along the (110) plane. It is also noteworthy that if the cutting process is continued layer by layer, the sequence of resulting terminations (3 and 4, 2 and 5, 1 and 6) becomes symmetrical up to permutation, consistent with the symmetry relations indicated in the scheme above.

Thus, when a crystal of $Be_{12}Ti$ is cleaved along a given crystallographic plane, two complementary surfaces are formed: one with relatively high surface energy and the other with a lower one. Consequently, the total energy required to create such cleavage corresponds to the average of the surface energies of these two surfaces. For instance, for the (110) plane, the calculated cleavage energies are 2.57 J/m^2 (terminations 6 and 1), 2.87 J/m^2 (terminations 5 and 2), and 2.65 J/m^2 (terminations 4 and 3). This demonstrates that the differences between the possible terminations of the (110) surface are minor, and the energy required to cleave the crystal of $Be_{12}Ti$ along this plane is nearly independent of the specific terminations formed.

Moreover, averaging over all terminations within a given surface orientation is equivalent to evaluating the average cleavage energy for that orientation. The resulting values are close to those discussed above and exhibit only weak variation between different orientations. Thus, for surfaces with high Miller indices, the anisotropy of the surface energy effectively vanishes. In this limit, orientation-independent average surface energy, $\bar{\gamma}$, can be used to estimate the equilibrium pressure in a spherical helium bubble of radius r using the classical relation $p = 2\bar{\gamma}/r$. Taking a helium bubble radius of $r = 5$ nm, as reported in Ref. [53], the corresponding internal pressure can reach up to 1.1 GPa. This value is significantly lower than the shear modulus μ of $Be_{12}Ti$, which typically lies in the range of 130-160 GPa. Therefore, under such conditions, dislocation loop punching is not expected in $Be_{12}Ti$.

3.4. Equilibrium crystal shape and Wulff polyhedra

The equilibrium crystal shape is determined using the classical Wulff construction. According to the Wulff theorem [54], the distance d_{hkl} from the crystal center to a facet with orientation (hkl) is proportional to its surface energy, $d_{hkl} = \lambda\gamma_{hkl}$, where λ is a scaling factor fixed by the crystal volume. In this geometrical construction, planes corresponding to different surface orientations are positioned at distances proportional to their respective surface energies, and the inner envelope of these planes defines the Wulff polyhedron. As a result, facets with lower surface energy extend farther from the center and occupy larger surface areas, whereas high-energy surfaces are truncated or may disappear entirely from the equilibrium shape. Thus, the relative surface area of each facet is inversely related to its surface energy: the lower the surface energy, the larger its contribution to the equilibrium crystal form. In the present work, only the zero-temperature limit is considered. Entropic and vibrational contributions are neglected, and the surface energy γ_{hkl} serves as the sole thermodynamic parameter governing the equilibrium shape. Notably, Wulff polyhedra describe not only the equilibrium shape of a crystal minimizing the total surface energy, but also the equilibrium shape of a pore or void corresponding to a minimum-energy surface configuration.

For beryllides, which possess complex crystal structures with multiple possible terminations for a single (hkl) surface, the choice of surface energy directly influences the predicted morphology. To assess this sensitivity, three limiting scenarios are examined: (i)

Wulff polyhedra are constructed using the lowest-energy termination for each orientation, corresponding to the thermodynamically most favorable configuration; (ii) Wulff polyhedra are generated using the highest-energy termination for each orientation, providing an upper-bound estimate of termination effects; (iii) an averaged surface energy, obtained by taking the mean over all terminations of a given orientation, is employed to construct an effective equilibrium shape. Comparison of these three cases at 0 K allows a systematic evaluation of the impact of termination-dependent surface energetics on the equilibrium crystal morphology.

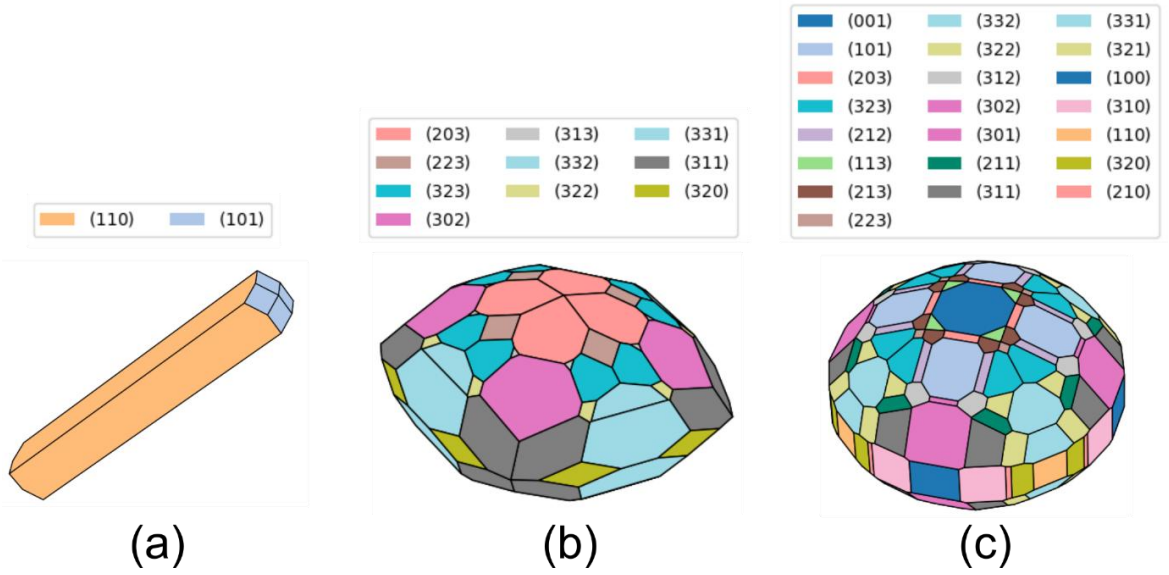

Fig. 5. Wulff polyhedra illustrating the equilibrium crystal shapes in $Be_{12}Ti$ obtained for three limiting scenarios. The polyhedra are constructed using (a) the lowest, (b) the highest, and (c) the termination-averaged surface energies for each surface.

The constructed Wulff polyhedra shown in Fig. 5 represent equilibrium shapes of crystals or pores in $Be_{12}Ti$ for three limiting scenarios. In the most realistic case, scenario (i), where the minimum-energy termination is adopted for each surface, the equilibrium shape is an elongated prism bounded by lateral (110) faces and convex bases composed of four (101) facets. This morphology is in good agreement with the shapes of bubbles, as well as with the reported width-to-height ratios for $Be_{12}Ti$ under neutron irradiation at 1040 K [55]. In that study, the bubbles were found to be decorated with silicon atoms, which can significantly modify surface energies and, consequently, affect the equilibrium bubble shape. Nevertheless, despite these additional effects, the agreement with the present results remains remarkably good. In contrast, the Wulff constructions for scenarios (ii) and (iii), based on the highest and averaged termination energies, differ markedly from scenario (i) and from each other. The polyhedron in Fig. 5b consists of ten facets with Miller indices equal to 3, whereas the polyhedron in Fig. 5c is composed of twenty-two distinct facets and closely resembles a spheroid, i.e., a sphere compressed along two opposite directions. As expected for an anisotropic material, the equilibrium shape deviates from a perfect sphere and corresponds to the configuration that minimizes the total surface energy, accounting for its dependence on surface orientation. This pronounced variation in equilibrium morphology highlights the strong sensitivity of the Wulff polyhedron to changes in the surface energies of its constituent facets. Such changes can arise, for example, from the adsorption of impurity atoms, which are inevitably present in real materials, as well as from variations in chemical environment.

The Wulff construction is traditionally used to describe equilibrium shapes that minimize the total surface energy of a crystal or a void and is strictly valid only under thermodynamic equilibrium conditions, where surface energies alone govern the morphology. In real materials, however, such equilibrium is rarely achieved. During irradiation at elevated temperatures, materials are driven far from equilibrium, and their microstructural evolution is governed by a complex interplay of kinetic and non-equilibrium processes. Under these conditions, the shape of voids is not determined solely by surface energy minimization, but by a balance between competing mechanisms such as defect production, diffusion, stress-driven mass transport, adsorption and desorption processes, and interactions with impurities or gas atoms. Moreover, the continuous incorporation of vacancies can remove successive surface layers, leading to transitions between different surface terminations. As a result, the observed void morphology may deviate substantially from the ideal Wulff shape. While the Wulff construction provides a useful reference for the equilibrium limit, realistic void shapes in dynamically evolving materials reflect the combined influence of non-equilibrium kinetics and local driving forces. Further kinetic Monte Carlo simulations are therefore required to more accurately describe the growth and evolution of helium bubbles.

The Allegro MLIAP, derived from *ab initio* calculations, will be further employed to investigate surface-related phenomena in $Be_{12}Ti$, which are critical for understanding its interaction with tritium. Under irradiation conditions, helium bubbles can nucleate and grow within the material, acting as trapping sites for radioactive tritium. The inner surface of such bubbles can be regarded as an effective free surface, where atomic tritium adsorbs and accumulates, leading to substantial modifications of surface energy and other surface-related properties. The use of MLIAP allows simulations of systems orders of magnitude larger than those accessible by first-principles methods while maintaining comparable accuracy. This approach substantially reduces computational cost and enables systematic, statistically meaningful studies of surfaces, defects, and irradiation-induced effects in $Be_{12}Ti$, which are essential for predicting its behavior in hydrogen-rich and radiation-intensive environments.

A detailed understanding of the energetics and atomic structure of free surfaces in $Be_{12}Ti$ is essential for predicting preferential adsorption and retention sites for tritium and other light species. Surface stability and termination are expected to strongly influence tritium accumulation at irradiation-induced cavities and bubbles. Quantitative estimates of tritium retention at such surfaces are therefore of high relevance for assessing the long-term safety, handling, and disposal of irradiated materials in nuclear and fusion applications.

4. Conclusions

This study presents *ab initio* calculations of the surface energies for 24 low-index crystallographic planes of intermetallic $Be_{12}Ti$ with indices ranging from 1 to 3 and their non-equivalent terminations. To accurately determine the chemical potentials of pure beryllium and titanium within $Be_{12}Ti$, a machine-learning interatomic potential was developed and trained on structures and atomic forces obtained from *ab initio* data. This potential enabled the accurate calculation of surface energies for non-stoichiometric slabs. The main findings are summarized as follows.

Surface relaxations of the selected (110) and (100) surfaces strongly depend on surface termination, showing complex inward and outward displacements of atomic layers determined by local atomic structure. Although relaxations generally decrease with depth and approach bulk-like behavior, some layers still show noticeable deviations, indicating that specific interlayer spacings remain highly sensitive to termination effects. The close agreement between the atomic displacements obtained from *ab initio* calculations and the Allegro MLIAP confirms

the reliability of the machine-learning potential in accurately reproducing surface relaxation effects.

The surface energy of $Be_{12}Ti$ is more strongly influenced by the atomic termination than by the crystallographic orientation of the plane, particularly for low-index surfaces. For surfaces with a maximum Miller index of 1, the surface energy exhibits a pronounced dependence on termination, reflecting the strong sensitivity of the system to the local atomic environment and surface composition. In contrast, for surfaces with maximum indices of 2 and 3, the variation in surface energy among different terminations is generally smaller, suggesting a diminishing influence of titanium atoms with increasing surface complexity. The surface energy reaches its maximum when titanium atoms are located deepest below the surface and its minimum when titanium atoms occupy the outermost atomic layer. This trend highlights the stabilizing role of surface titanium atoms.

The equilibrium crystal and void morphologies of $Be_{12}Ti$ are shown to be highly sensitive to termination-dependent surface energetics, as demonstrated through Wulff constructions based on different limiting surface-energy scenarios. While the lowest-energy terminations produce equilibrium shape consistent with experimentally observed irradiation-induced bubbles, substantial variations in morphology arise when higher or averaged surface energies are considered.

The combination of a high-throughput workflow with a machine-learning interatomic potential provides a robust framework for assessing tritium retention on $Be_{12}Ti$ surfaces. After incorporating helium and hydrogen interactions, this approach will enable large-scale simulations of helium bubble formation and tritium trapping at their surfaces in $Be_{12}Ti$. Such modeling is essential for evaluating the total tritium inventory in neutron multiplier components employed in fusion reactors and will be addressed in subsequent publications.

Conflict of interest

The authors declare that they have no known competing financial interests or personal relationships that could have appeared to influence the work reported in this paper.

Data Availability

The raw/processed data required to reproduce these findings cannot be shared at this time as the data was obtained within the frames of the EUROfusion project.

CRediT authorship contribution statement

D.V. Bachurin: Conceptualization, Data curation, Formal analysis, Investigation, Validation, Visualization, Writing - original draft, Writing- Reviewing and Editing. **C. Stihl:** Data curation, Formal analysis, Methodology, Validation, Visualization, Writing - original draft. **P.V. Vladimirov:** Conceptualization, Funding acquisition, Methodology, Resources, Software, Supervision, Validation, Writing- Reviewing and Editing.

Acknowledgements

This work has been carried out within the framework of the EUROfusion Consortium, funded by the European Union via the Euratom Research and Training Programme (Grant Agreement No 101052200 — EUROfusion). Views and opinions expressed are however those of the author(s) only and do not necessarily reflect those of the European Union or the European Commission. Neither the European Union nor the European Commission can be held responsible for them. High-performance computing resources were provided by the

EUROfusion and performed at the High-Performance Computers Marconi-Fusion (Bologna, Italy).

References

[1] P.S. Maiya, J.M. Blakely, Surface Self-Diffusion and Surface Energy of Nickel, J Appl Phys 38(2) (1967) 698-704.
[2] E. Preuss, N. Freyer, H.P. Bonzel, Surface Self-Diffusion on Pt(110) - Directional Dependence and Influence of Surface-Energy Anisotropy, Appl Phys a-Mater 41(2) (1986) 137-143.
[3] B. Li, X. Li, W. Gao, Q. Jiang, An effective scheme to determine surface energy and its relation with adsorption energy, Acta Mater 212 (2021) 116895.
[4] J.C. Tracy, Structural Influences on Adsorption Energy. 3. CO on Cu(100), J Chem Phys 56(6) (1972) 2748-2754.
[5] J. Feng, J.M. Slocik, M. Sarikaya, R.R. Naik, B.L. Farmer, H. Heinz, Influence of the Shape of Nanostructured Metal Surfaces on Adsorption of Single Peptide Molecules in Aqueous Solution, Small 8(7) (2012) 1049-1059.
[6] N.H. Heo, K.H. Chai, J.G. Na, Correlation between interfacial segregation and surface-energy-induced selective grain growth in 3% silicon-iron alloy, Acta Mater 48(11) (2000) 2901-2910.
[7] P. Moazzam, G. Luciano, A. Razmjou, E. Akbari, P.G. Ul'yanov, S. Mahanty, Effect of molecular-scale surface energy alteration of aluminium on its corrosion resistance behaviour, Colloid Surface A 562 (2019) 26-33.
[8] J. Xia, G.M. Zhu, X.J. Gao, S. Wang, Z. Chang, N.A. Guo, J.H. Ding, X.Q. Zhai, X.D. Li, Research on surface energy and corrosion resistance by electrochemical processing of 304-Cu stainless steel, Mater Today Commun 39 (2024) 108847.
[9] W. Li, D.Y. Li, Influence of surface morphology on corrosion and electronic behavior, Acta Mater 54(2) (2006) 445-452.
[10] X.Y. Li, H.S. Cheng, F.J. Yang, Radiation-Induced Damage in Gap by Mev Helium-Ions, Acta Phys Sin-Ov Ed 3(2) (1994) 116-123.
[11] W.B. Liu, N. Wang, Y.Z. Ji, P.C. Song, C. Zhang, Z.G. Yang, L.Q. Chen, Effects of surface energy anisotropy on void evolution during irradiation: A phase-field model, J Nucl Mater 479 (2016) 316-322.
[12] Q.F. Feng, Y.P. Yin, W.T. Han, X.O. Yi, P.P. Liu, R. Kasada, S. Ohnuki, F.R. Wan, Surface-Driven Anomalies in irradiation Damage: Low swelling in 316LN stainless steel under Gold-Ion irradiation up to 290 dpa, Appl Surf Sci 703 (2025) 163437.
[13] P. Vladimirov, D. Bachurin, V. Borodin, V. Chakin, M. Ganchenkova, A. Fedorov, M. Klimenkov, I. Kupriyanov, A. Moeslang, M. Nakamichi, T. Shibayama, S. Van Til, M. Zmitko, Current Status of Beryllium Materials for Fusion Blanket Applications, Fusion Sci Technol 66(1) (2014) 28-37.
[14] P.V. Vladimirov, V.P. Chakin, M. Durrschnabel, R. Gaisin, A. Goraieb, F.A.H. Gonzalez, M. Klimenkov, M. Rieth, R. Rolli, N. Zimber, S. Udartsev, M. Kolmakov, A. Vechkutov, E. Frants, Development and characterization of advanced neutron multiplier materials, J Nucl Mater 543 (2021) 152593.
[15] Y. Fujii, M. Miyamoto, J.-H. Kim, M. Nakamichi, N. Murayoshi, H. Iwakiri, Hydrogen retention behavior of beryllides as advanced neutron multipliers, Nucl Mater Energy 9 (2016) 233-236.
[16] R. Gaisin, Y. Frants, M. Kolmakov, B. Zorin, M. Kylyshkanov, M. Podoinikov, S. Udartsev, A. Vechkutov, V. Chakin, P. Vladimirov, Beryllium intermetallics: Industrial experience on development and manufacture, Nucl Mater Energy 35 (2023) 101444.

[17] J.-H. Kim, T. Hwang, Y. Sugimoto, M. Nakamichi, M. Miyamoto, Deuterium retention properties of vanadium beryllide (Be12V) for advanced neutron multiplier applications, Fusion Eng Des 201 (2024) 114278.
[18] D.V. Bachurin, P.V. Vladimirov, Ab initio study of Be and Be12Ti for fusion applications, Intermetallics 100 (2018) 163-170.
[19] D.V. Bachurin, C. Stihl, P.V. Vladimirov, Ab initio study of hydrogen diffusion in Be and Be12Ti for fusion applications, Comp Mater Sci 187 (2021) 109921.
[20] L. Song, A.C. Shao, D. Li, X.L. Tian, Z.H. Qiao, H.G. Tang, X.H. Lin, First-principles study for quasi-static growth model in FeAl intermetallic based on Wulff cluster model, Rsc Adv 14(12) (2024) 8116-8123.
[21] M. Krajcí, J. Hafner, Surfaces of intermetallic compounds: An DFT study for B20-type AlPd, Phys Rev B 87(3) (2013) 035436.
[22] Z. Jiao, Q.J. Liu, F.S. Liu, B. Tan, Structural and electronic properties of low-index surfaces of NbAl intermetallic with first-principles calculations, Appl Surf Sci 419 (2017) 811-816.
[23] S.P. Sun, X.P. Li, H.J. Wang, H.F. Jiang, W.N. Lei, Y. Jiang, D.Q. Yi, First-principles investigations on the electronic properties and stabilities of low-index surfaces of L1-AlSc intermetallic, Appl Surf Sci 288 (2014) 609-618.
[24] B.J. Morgan, J. Carrasco, G. Teobaldi, Variation in surface energy and reduction drive of a metal oxide lithium-ion anode with stoichiometry: a DFT study of lithium titanate spinel surfaces, J Mater Chem A 4(43) (2016) 17180-17192.
[25] W.H. Sun, G. Ceder, Efficient creation and convergence of surface slabs, Surf Sci 617 (2013) 53-59.
[26] R. Tran, Z.H. Xu, B. Radhakrishnan, D. Winston, W.H. Sun, K.A. Persson, S.P. Ong, Surface energies of elemental crystals, Sci Data 3 (2016) 160080.
[27] G. Kresse, D. Joubert, From ultrasoft pseudopotentials to the projector augmented-wave method, Phys Rev B 59(3) (1999) 1758-1775.
[28] J.P. Perdew, K. Burke, M. Ernzerhof, Generalized gradient approximation made simple, Phys Rev Lett 77(18) (1996) 3865-3868.
[29] J.W. Furness, A.D. Kaplan, J.L. Ning, J.P. Perdew, J.W. Sun, Accurate and Numerically Efficient rSCAN Meta-Generalized Gradient Approximation, J Phys Chem Lett 11(21) (2020) 9248-9248.
[30] https://next-gen.materialsproject.org/materials/mp-1104067/tasks/mp-2024836.
[31] Jmol: an open-source Java viewer for chemical structures in 3D. http://www.jmol.org/.
[32] A. Musaelian, S. Batzner, A. Johansson, L.X. Sun, C.J. Owen, M. Kornbluth, B. Kozinsky, Learning local equivariant representations for large-scale atomistic dynamics, Nat Commun 14 (2023) 579.
[33] S. Batzner, A. Musaelian, L.X. Sun, M. Geiger, J.P. Mailoa, M. Kornbluth, N. Molinari, T.E. Smidt, B. Kozinsky, E(3)-equivariant graph neural networks for data-efficient and accurate interatomic potentials, Nat Commun 13 (2022) 2453.
[34] C.W. Tan, M.L. Descoteaux, M. Kotak, G.M. Nascimento, S.R. Kavanagh, L. Zichi, M. Wang, A. Saluja, Y.R. Hu, T. Smidt, A. Johansson, W.C. Witt, B. Kozinsky, A. Musaelian, High-performance training and inference for deep equivariant interatomic potentials, arXiv preprint arXiv:2504.16068 (2025).
[35] D.V. Bachurin, P.V. Vladimirov, Ab initio study of hydrogen on beryllium surfaces, Surf Sci 641 (2015) 198-203.
[36] D.V. Bachurin, P.V. Vladimirov, Ab initio study of beryllium surfaces with different hydrogen coverages, Acta Mater 134 (2017) 81-92.

[37] S.J. Tang, H.T. Jeng, C.S. Hsue, Ismail, P.T. Sprunger, E.W. Plummer, Surface state influence on the surface lattice structure in Be(10(1)over-bar0), Phys Rev B 77(4) (2008) 045405.
[38] Ismail, P. Hofmann, A.P. Baddorf, E.W. Plummer, Thermal expansion at a metal surface: A study of Mg(0001) and Be(10(1)over-bar0), Phys Rev B 66(24) (2002) 245414.
[39] M. Lazzeri, S. de Gironcoli, First-principles study of the thermal expansion of Be(10(1)over-bar0), Phys Rev B 65(24) (2002) 245402.
[40] P. Hofmann, K. Pohl, R. Stumpf, E.W. Plummer, Geometric structure of Be(10(1)over-bar-0), Phys Rev B 53(20) (1996) 13715-13719.
[41] E. Wachowicz, A. Kiejna, Multilayer relaxations at the (0001) surface of Be and Mg, Solid State Commun 116(1) (2000) 17-20.
[42] M. Lazzeri, S. de Gironcoli, Ab-initio dynamical properties of the Be(0001) surface, Surf Sci 402(1-3) (1998) 715-718.
[43] P.J. Feibelman, Relaxation of hcp(0001) surfaces: A chemical view, Phys Rev B 53(20) (1996) 13740-13746.
[44] M.N. Huda, L. Kleinman, Density functional calculations of the influence of hydrogen adsorption on the surface relaxation of Ti(0001), Phys Rev B 71(24) (2005) 241406.
[45] G. Teeter, J.L. Erskine, Surface relaxation of Ti(0001): Influence of hydrogen contamination, Phys Rev B 61(20) (2000) 13929-13935.
[46] P. Jiang, P.M. Marcus, F. Jona, Relaxation at Clean Metal-Surfaces, Solid State Commun 59(5) (1986) 275-280.
[47] J. Sokolov, F. Jona, P.M. Marcus, Trends in Metal-Surface Relaxation, Solid State Commun 49(4) (1984) 307-312.
[48] N. Kumar, P. Ghosh, Structure and stability of clean and adsorbate covered intermetallic PdGa surfaces: A first principles study, Surf Sci 644 (2016) 69-79.
[49] W. Li, X.H. Peng, A.H.W. Ngan, J.A. El-Awady, Surface energies and relaxation of NiCoCr and NiFeX (X = Cu, Co or Cr) equiatomic multiprincipal element alloys from first principles calculations, Model Simul Mater Sc 30(2) (2022) 025001.
[50] E.C. Zuo, X.L. Dou, Y.Y. Chen, W.J. Zhu, G. Jiang, A.J. Mao, J.G. Du, Electronic work function, surface energy and electronic properties of binary Mg-Y and Mg-Al alloys: A DFT study, Surf Sci 712 (2021) 121880.
[51] Y. Zhou, H.H. Xiong, Y.H. Yin, S.W. Zhong, First principles study of surface properties and oxygen adsorption on the surface of Al3Ti intermetallic alloys, Rsc Adv 9(4) (2019) 1752-1758.
[52] N. Li, C.F. Dong, X. Wei, C. Man, J.Z. Yao, J.L. Cao, X.G. Li, Scanning Kelvin Probe Force Microscopy and Density Functional Theory Studies on the Surface Potential of the Intermetallics in AA7075-T6 Alloys, J Mater Eng Perform 28(7) (2019) 4289-4301.
[53] Y. Sugimoto, M. Miyamoto, J.H. Kim, T. Hwang, M. Nakamichi, Helium swelling behavior for neutron multipliers after irradiation with He ions at high temperatures, Nucl Mater Energy 38 (2024) 101584.
[54] G. Wulff, Zur Frage der Geschwindigkeit des Wachsthums und der Auflösung der Krystallflachen, Zeitschrift für Krystallographie und Mineralogie 34(5/6) (1901) 449-530.
[55] V. Chakin, R. Rolli, H.C. Schneider, R. Gaisin, P. Vladimirov, M. Klimenkov, M. Duerrschnabel, N. Zimber, M. Rieth, B. Gorr, F.A. Hernández, D. Radloff, A. Fedorov, M. Zmitko, M. Nakamichi, S. Udartsev, High-dose neutron irradiation of beryllium and titanium beryllide: Summary and outlook, Nucl Mater Energy 42 (2025) 101910.